Transport phenomena in a parallel passage reactor

A1

67C

Transport phenomena in a parallel passage reactor

J.H.B.J. Hoebink, E.P.J. Mallens, K.A. Vonkeman* and G.B. Marin

Eindhoven University of Technology
Laboratorium voor Chemische Technologie
P.O. Box 513
5600 MB Eindhoven
The Netherlands

*Koninklijke/Shell Laboratorium, Amsterdam
P.O. Box 3003
1003 AA Amsterdam
The Netherlands

Prepared for presentation at the AIChE 1993 Spring National Meeting
March 28 - April 1, 1993, Houston

Petroleum Processes Session

1. Introduction

A parallel passage reactor or PPR is a continuous flow reactor, made up of alternating empty or catalyst containing sections parallel to the flow direction. The sections are separated by gauze, allowing mass transfer between them. The empty and catalytic spaces may be arranged as parallel slabs. Alternatively, the empty channels may be surrounded by catalyst particles. This latter configuration resembles the well-known catalytic monolith reactor.

When properly designed the major gas flow, which passes the empty space, contacts the catalyst sufficiently to reach any desired conversion of reactants, while the pressure drop across the reactor is small when compared to normal fixed bed reactors. The main application area concerns the treatment of dusty stack gases, for which traditional fixed beds are unsuitable, since the dust particles settle inside the packing, resulting in a gradually increasing pressure drop which requires a regular shut-down of the reactor for cleaning purposes. A PPR avoids these problems. As such this type of reactor was originally developed for the Shell Flue Gas Desulphurisation Process (Pohlenz [1984]).

The current investigation deals with aspects of heat and mass transfer in a PPR consisting of parallel empty channels in a catalyst bed.

2. Experimental set-up and methods.

2.1 General aspects.

For the experiments a model version of the PPR was used, which consisted of a single empty gauze channel surrounded by a catalyst bed. The reactor consisted of a regular prism of 5x5x50 cm with a widening entry zone and a narrowing exit zone, all walls being made of aluminum. Inside the reactor a single, axially directed gauze channel, 50 cm long, was maintained in the center by means of connections to two gauze planes of 5x5 cm at the entrance and exit of the prism, see Figure 1. Gauze channels with triangular, rectangular and circular cross-sections were investigated. The hydraulic diameter amounted to 6 mm in each case.

Three different particle shapes were investigated: spheres, trilobes and granules with equivalent diameters of 3 mm, 1.6 mm and 1.1 mm, and corresponding bed porosities of 0.42, 0.52 and 0.40. During all experiments nitrogen flowed through the reactor. The flowrate was adjusted with a needle valve and measured with a rotameter. Experiments were performed at either a low gas flow velocity of about 7 $m_g\ s^{-1}$ or a high velocity of about 20 $m_g\ s^{-1}$ through the channel, which are values for industrial application of a PPR. The gas flow velocity in the channel was obtained from the total flowrate corrected for the flowrate through the bed.

The latter was measured via tracer experiments. Oxygen was used as tracer gas. Tracer injections were either pulse wise or continuous, and the flowrate through the injection capillary was always adjusted to the local flowrate. The exit of the injection capillary was bent into the direction of the main stream through the reactor. The reactor wall contained connection points at different axial positions allowing insertion of capillaries for injection of tracer gases or for sampling of the gas phase. The radial position for injection or sampling could be varied from the wall of the reactor to the inside of the empty channel.

The tracer concentration was measured via the sampling capillaries, which were connected by means of a multi-channel injection valve to a quadrupole mass-spectrometer. The reactor was fully insulated in order to approach adiabatic operation during the heat transfer experiments.

The transport parameters were estimated from the experimental data by means of a Marquardt [1963] routine for non-linear single response regression.

2.2 Velocity inside the catalyst bed.

The importance of entrance effects was determined qualitatively by pulse injections of oxygen in the middle between the channel and the reactor wall at 5 cm from the entrance of the packed region, followed by detection at 7 and 13 cm from the injection point at various distances between channel and reactor wall.

The radial velocity profile was measured outside the region with entrance effects by oxygen pulse injections at 25 cm from the entrance and at various radial positions, followed by detection at 12 cm from the injection point and at the same radial positions. The linear gas flow velocity was calculated from the distance between injection and detection points and the time interval between detection and injection, after appropriate correction for the delay in the injection and detection lines. The superficial gas flow velocity was calculated from the linear gas flow velocity by multiplying with the bed porosity.

2.3 Mass transport and transfer.

In order to assess the importance of mass transport and transfer resistances, oxygen was injected continuously in the upper corner of the gauze channel at 22 cm downstream from the entrance. The steady state radial concentration profile was measured at 2.5 and 23 cm downstream from the injection point.

During measurements of the effective radial diffusion coefficients the gauze channel was covered with an aluminum foil from 22 cm of the entrance until the end of the packing to avoid a non-uniform radial velocity profile inside the bed, which would cause local variations of the diffusion coefficients. For determination of the effective radial diffusion coefficient a continuous oxygen injection was performed at 36 cm from the entrance and 1 cm from the wall. The steady state oxygen concentration was measured 2 cm downstream of the injection at various radial positions. The linear gas flow velocity was determined as described in 2.2.

2.4 Heat transport and transfer.

Transient heating of the reactor was performed at a velocity of 20 m s^{-1} in the channel, with trilobes as packing material. The gas feed, preheated with resistance wire, by-passed the reactor until a constant feed temperature of 773 K was reached. At time t=0 the gas was sent through the reactor and temperatures as function of time were recorded, using thermocouples inserted into the catalyst bed through the wall of the reactor at various axial and radial positions. It was assumed that the measured temperature is the solid phase temperature.

In spite of extensive heat insulation the reactor failed to be adiabatic, as indicated by the development of an axial temperature profile in the steady state. Therefore the data analysis was restricted to the temperatures observed at 5 cm from the entrance of the bed and during the first 120 seconds of the heating period, i.e. at a position and at times corresponding to adiabatic operation.

3. Results and discussion

3.1 Entrance effects and radial velocity profile in the bed

From the measurements concerning the entrance effects a typical profile of the observed maximum oxygen concentration at the sampling points is shown in Figure 2. A triangular gauze channel was used during the experiments. At 12 cm from the bed's entrance concentrations become higher when the sampling point approaches the channel. It indicates that the axial flow pattern is not yet fully developed, and that some flow towards the gas channel occurs. At an axial position of 18 cm an opposite trend is found, which can be understood from the high superficial velocities near the gauze, as discussed below.

Similar results were obtained with spheres, and with a low velocity in the channel. In general the entrance effects disappeared between 12 and 20 cm from the bed's entry.

Fully developed radial velocity profiles are shown in Figures 3 and 4 as superficial velocity versus the distance from the channel. High velocities are observed near the gas channel and a steep gradient exists up to 1 cm from the gauze. A higher velocity in the channel causes higher velocities in the bed near the channel, see Figure 4, but hardly affects the velocities at larger distances from the channel.

Apparently momentum is transfered from the channel gas flow to the surface of the particles in the neighbourhood of the channel, which causes the increase of the velocity in comparison to more remote regions. The larger packing porosity at the channel/bed interface certainly will enhance this effect.

Trilobes and spheres show qualitatively similar results, although the absolute values of the velocities tend to differ at higher channel gas velocity.

At the conditions corresponding to Figure 4 for the spherical particles the mean superficial gas flow velocity in the bed amounts 0.06 $m_g^3\ m_b^{-2}\ s^{-1}$. A separate experiment was performed without a channel present in the reactor, during which experiment the gasflow was adjusted until the pressure drop was equal to the one with the channel present, i.e. 0.6 kPa. The gas flowrate corresponded to a superficial gas flow velocity of 0.05 $m_g^3\ m_b^{-2}\ s^{-1}$, which agrees with the mean superficial gas flow velocity in the presence of a channel.

3.2 Mass transport and transfer resistances

In general one can distinguish several potential transport resistances in series for a PPR, which are shown in Table 1. A mass transfer coefficient is a priori calculated from literature correlations for each resistance, assuming a velocity of 20 m s^{-1} in the empty channels. The calculated mass transfer coefficients are shown in Table 1.

According to Table 1, the relevant transport resistances in a PPR are mass transport through the gauze wall, mass transfer from the gauze wall to the bed and mass transport inside the bed.

Table 1: Potential transport resistances in a PPR and a priori estimates for the corresponding mass transfer coefficients [1]

transport resistance	k / m_r s^{-1}
from the bulk of the channel to the gauze wall [2]	$3\ 10^{-1}$
at the gauze wall [3]	$5\ 10^{-3}$
from the gauze wall to the bed [4]	$4\ 10^{-3}$
inside the bed [5]	$2\ 10^{-3}$
from the bulk gas in the bed to the external surface of the particles [6]	$1\ 10^{-1}$
inside the particle [7]	$1\ 10^{-2}$

[1] calculations were performed for nitrogen as fluid and a temperature of 298 K

[2] the mass transfer relation is derived from the pressure drop correlation of Ergun [1952] for the gas channel using the Reynolds analogy. The friction factor was estimated from pressure drop measurements on a commercial PPR. The hydraulic channel diameter is 6 mm and the channel gas flow velocity is 20 m s^{-1}

[3] the mass transfer coefficient is calculated from the molecular diffusion coefficient, multiplied by the open surface fraction of the gauze (0.5) and divided by the gauze wire thickness (1 mm)

[4] the mass transfer relation is derived from the correlation of Li and Finlayson [1977] for heat transfer in packed tubes, using the analogy between heat and mass transfer. The chosen particle diameter is 3 mm and a linear gas flow velocity of 0.14 m s^{-1} inside the bed is applied

[5] the mass transfer coefficient is calculated from the effective radial diffusion coefficient divided by the hydraulic bed diameter for a commercial PPR. The stagnant contribution to the effective radial diffusion coefficient is equal to the effective molecular diffusion coefficient. The dynamic contribution to the effective radial diffusion coefficient was calculated from the superficial gas flow velocity, which is multiplied by an experimentally determined mixing length. The particle diameter is 3 mm and a linear gas flow velocity of 0.14 m s^{-1} inside the bed is applied

[6] the mass transfer relation is derived from the pressure drop correlation of Ergun [1952] using the Reynolds analogy. The particle diameter is 3 mm and a linear gas flow velocity of 0.14 m s^{-1} inside the bed is applied

[7] the mass transfer coefficient is calculated from the effective intraparticle diffusion coefficient, multiplied by the shape factor for spheres (10) and divided by the particle diameter (3 mm)

The experimental results concerning mass transfer between the channel and the bed are presented as steady state radial concentration profiles at two different axial positions. All results refer to granules. It is reminded that during these experiments the tracer was continuously fed in the upper corner of the channel. Figures 5 and 6 show data at low and high channel velocity in a channel of triangular shape. Figure 7 concerns a circular duct at low velocity.

Both Figures 5 and 6 clearly illustrate that considerable mass transfer resistance exists inside the triangular channel. When comparing Figures 5 and 6, this resistance is less at high velocity in the channel since the profile is less pronounced at larger axial positions. However when a circular channel is applied, see Figure 7, the channel-to-gauze wall resistance is seriously reduced as indicated by the rather flat radial concentration profiles at the largest axial position.

The difference in mass transfer resistance between triangular and circular ducts results from the thick boundary layers that can be expected to exist in the corner regions of the triangular channel because of wall effects. Such layers form a considerable diffusion barrier. In the circular channel turbulent flow will be fully developed and any laminar layer will contribute much less to mass transfer resistance.

Similar experiments were performed with a rectangular channel, and with trilobes and spheres as packing material. The results confirm that corners in the cross-section of the duct should be avoided, as they contribute much to the total resistance to radial transport.

Contrary to the a priori estimates for transport resistances in a PPR, presented in Table 1, the results in Figures 5, 6 and 7 express that the mass transport resistance of the gauze wall can be neglected as concentrations on both sides of the wall are hardly different.

Also mass transfer resistance from the gauze wall to the bed is of minor importance. This is explained with the transfer of momentum from the channel to the bed, discussed in 3.1, which strongly enhances mass transport through the gauze wall and mass transfer from the gauze wall to the bed.

When circular ducts are applied the main transport resistance is located inside the fixed bed due to a limited radial dispersion. This is quantified in the next section.

A typical steady state radial concentration profile, as measured in experiments on the estimation of the effective radial diffusion coefficient, is shown in Figure 8 for trilobes as packing material and a low flow gas velocity. The full curve in Figure 8 corresponds to regression of the data to the model of Bischoff and Levenspiel [1962 A], Equation 1 to 3.

$$\Phi = 1 + 0.5 \sum_{a_i>0} q^{-1} \exp\left[(0.5 - q)\, Pe_{L,r}\, \Psi\right] \frac{J_o(a_i \lambda)}{J_o^2(a_i)} \qquad \text{Eq. 1}$$

in which:

$$J_1(a_i) = 0 \qquad \text{Eq. 2}$$

$$q = \sqrt{\left(0.25 + \frac{a_i^2}{Pe_{L,r} + Pe_{R,r}}\right)} \qquad \text{Eq. 3}$$

with Ψ as the dimensionless axial position, λ as the dimensionless radial position and Φ as the dimensionless tracer concentration.

This equation follows from the integration of the continuity equation for the tracer. The tube diameter dimension to be substituted into the model equations 1 to 3 is chosen at two centimetre.

The estimated effective radial diffusion coefficients are shown in Table 2. When applying the model the values for the effective axial diffusion coefficient were calculated from the work of Bischoff and Levenspiel [1962 B]. These values had no effect on the observed estimates for the effective radial diffusion coefficients.

Gunn [1987] presented correlations for the calculation of effective radial diffusion coefficients in classical fixed beds:

$$\frac{1}{Pe_r} = \frac{1}{Pe_f} + \frac{\varepsilon}{\tau\, Re\, Sc} \qquad \text{Eq. 4}$$

where Pe_f is the fluid mechanical Péclet number for radial dispersion estimated from the following equations (Gunn [1987]):

$$Pe_f = 40 - 29 \exp\left(\frac{-7}{Re}\right) \;;\; \tau = 1.2 \qquad \textit{spheres} \qquad \text{Eq. 5}$$

$$Pe_f = 11 - 4 \exp\left(\frac{-7}{Re}\right) \;;\; \tau = 1.93 \qquad \textit{cylinders} \qquad \text{Eq. 6}$$

Comparing the present results to those from the literature, see Table 2, shows good agreement, meaning that effective radial diffusion coefficients in PPR reactors may be calculated from literature correlations for fixed beds.

Table 2: Estimated effective radial diffusion coefficients by regression of the data to the model (Equation 1 to 3) and values calculated according to the correlations of Gunn [1987] (Equation 4 to 6)

particle shape	estimated D_r / 10^{-5} m_r^2 s^{-1} 95 % probability level		D_r / 10^{-5} m_r^2 s^{-1}
	lower limit	upper limit	Gunn [1987]
sphere [1]	4.3	11.0	4.2
trilobe [2]	1.1	1.7	1.5
trilobe [3]	5.1	8.6	5.1

[1] $v = 1.4\ 10^{-1}\ m_r\ s^{-1}$

[2] $v = 3.4\ 10^{-2}\ m_r\ s^{-1}$

[3] $v = 1.7\ 10^{-1}\ m_r\ s^{-1}$

3.3 Heat transport and transfer resistances

The transient heating of the model PPR was simulated with a two-dimensional model, in which the following assumptions were made:

- unsteady state behaviour;
- adiabaticity;
- plug flow in the channel;
- convective axial heat transport, both in the channel and in the bed;
- axial conduction is neglected, both in the channel and in the bed, when compared to convective axial heat transport;
- uniform radial temperature profile in the channel;
- heat transfer resistances between the channel and the bed are neglected;
- radial heat conduction in the bed;
- heat transfer at a finite rate between gas and particles inside the bed;
- uniform particle temperature.

Since radial temperature gradients inside the channel are neglected, the radial coordinate x is only referring to the bed. The contact area between channel and bed is the radial position x=0 and the contact area between bed and reactor wall is the radial position x=B.

The energy balance for the gas in the channel is given by:

$$-G_c A_c C_{p,g} \frac{\partial T_c}{\partial z} - S_c \phi_t = A_c \rho_g C_{p,g} \frac{\partial T_c}{\partial t} \qquad \text{Eq. 7}$$

The energy balance for the gas inside the bed is given by:

$$-G_b C_{p,g} \frac{\partial T_b}{\partial z} + \lambda_{er} \frac{\partial^2 T_b}{\partial x^2} - (1-\varepsilon)\, \alpha_{g,s} S_b (T_b - T_s) = \varepsilon \rho_g C_{p,g} \frac{\partial T_b}{\partial t} \qquad \text{Eq. 8}$$

Finally, the energy balance for the solids in the bed takes into account the heating of the particles:

$$\alpha_{g,s} S_b (T_b - T_s) = \rho_s C_{p,s} \frac{\partial T_s}{\partial t} \qquad \text{Eq. 9}$$

The following initial and boundary conditions were used.

Initially, all gas temperatures are equal to the temperature of the surroundings:

$$T_b = T_r \quad 0 \le x \le B,\ 0 \le z \le L,\ t = 0$$
$$T_c = T_r \quad x = 0,\ 0 \le z \le L,\ t = 0 \qquad \text{Eq. 10}$$
$$T_s = T_r \quad 0 \le x \le B,\ 0 \le z \le L,\ t = 0$$

At the reactor entrance the gas temperature in both the channel and the bed are equal to the temperature of the heated gas at times larger than zero:

$$T_b = T_o \quad 0 \le x \le B,\ z = 0,\ t > 0$$
$$T_c = T_o \quad x = 0,\ z = 0,\ t > 0 \qquad \text{Eq. 11}$$

From the assumption of adiabaticity it follows:

$$\frac{\partial T_b}{\partial x} = 0 \quad 0 < z \le L,\ x = B,\ t > 0 \qquad \text{Eq. 12}$$

The remaining boundary conditions follow from the analogy between heat and mass transfer and the results concerning the latter, see section 3.2:

$$T_b = T_c \quad 0 \le z \le L,\ x = 0,\ t > 0 \qquad \text{Eq. 13}$$

$$\phi_t = -\lambda_{er}\left(\frac{\partial T_b}{\partial x}\right)_{x=0} \quad 0 < z \le L,\ x = 0,\ t > 0 \qquad \text{Eq. 14}$$

The model equations were solved with routine D02NGF from the NAG-library [1991], which applies backwards differentiation.

In Figure 9 the data points correspond to typical observed solid phase temperatures versus time, while the full curve corresponds to regression of the complete set of experimental data to the model (Equation 7 to 14). The estimated parameter values for the superficial mass flow velocity inside the bed G_b , the effective radial thermal conductivity λ_{er} and the overall fluid-solid heat transfer coefficient $\alpha_{g,s}$, are shown in Table 3. The agreement between experimental and predicted temperature profile is satisfactory.

The estimates obtained for the effective radial thermal conductivity and the overall fluid-solid heat transfer coefficient have been compared to correlations from the literature for fixed beds. Yagi and Kunii [1957] and Kunii and Smith [1960] recommend the following relation for the static contribution to the effective radial thermal conductivity, λ°_{er} :

$$\frac{\lambda^{\circ}_{er}}{\lambda_g} = \varepsilon\left(1 + \frac{\beta\, d_p\, \alpha_{rv}}{\lambda_g}\right) + \frac{\beta\,(1-\varepsilon)}{\left(\frac{1}{\frac{1}{\varphi} + \frac{\alpha_{rs}\, d_p}{\lambda_g}}\right) + \left(\gamma\frac{\lambda_g}{\lambda_s}\right)} \qquad \text{Eq. 15}$$

Neglecting the radiative contributions from the gas and the solids, expressed as α_{rg} and α_{rs} respectively, using the following data: $\lambda_g = 0.05$ W m^{-1} K^{-1}, $\lambda_s = 1.7$ W m$_p^{-1}$ K^{-1}, $\varepsilon = 0.5$, $\beta = 0.9$, $\varphi = 0.3$, $\gamma = 2/3$, results for the static contribution to the effective radial thermal conductivity to the value shown in Table 3, which agrees fairly well with the value estimated from the present experiments.

The gas film heat transfer coefficient, taking into account the heat transfer resistance over the film surrounding the particle, was calculated from the correlation of Handley and Heggs [1968]:

$$Nu = \frac{0.255}{\varepsilon}\, Re^{0.67}\, Pr^{0.33} \qquad \text{Eq. 16}$$

$$\text{for } Re > 100 \quad \text{and} \quad \frac{d_t}{d_p} > 8$$

The overall fluid-solid heat transfer coefficient was estimated from a relation presented by Stuke [1948]:

$$\frac{1}{\alpha_{g,s}} = \frac{1}{\alpha_g} + \frac{d_p}{\beta \lambda_s} \qquad \text{Eq. 17}$$

with β = 10 for spheres, 8 for cylinders and 6 for slabs.

The calculated overall fluid-solid heat transfer coefficient from Equation 17 with parameter values α_g = 63 W m_p^{-2} K (Equation 16), d_p = 1.6 10^{-3} m_p, λ_s = 1.7 W m_p^{-1} K and β=8, is shown in Table 3 and there is a significant difference with the value estimated from the experiment. However, according to Dixon and Cresswell [1979] estimates for the film heat transfer coefficient show much scattering at low Reynolds numbers, which in our case amounts to fifteen.

The intraparticle heat transport resistance, given by $d_p \beta^{-1} \lambda_s^{-1}$, can be compared to the overall fluid-solid heat transfer resistance, given by $\alpha_{g,s}^{-1}$. Substituting the values of β, d_p and λ_s shown above and the estimated value for $\alpha_{g,s}$, shown in Table 3, shows that the intraparticle heat transfer resistance is negligible.

The relative importance of heat transport resistance inside the bed of a PPR can be determined by multiplying the estimated effective radial thermal conductivity of Table 3 with the reciprocal value of the hydraulic bed diameter for a commercial PPR, which results in a value of 9.3 W m_p^{-2} K^{-1} for the equivalent bed heat transfer coefficient. Comparing this value to the estimated overall fluid-solid heat transfer coefficient, given in Table 3, shows that the resistances for heat transport inside the bed and heat transfer for the film surrounding the particle are comparable.

Table 3: Estimated heat transport parameters by regression of the complete set of experimental data to the model (Equation 7 to 14) and values calculated from literature correlations (Equation 15 to 17)

parameter	estimated value 95 % probability level lower limit	upper limit	literature
G_b / kg m_b^{-2} s^{-1}	0.16	0.19	-
λ_{er} / W m_b^{-1} K^{-1}	0.12	0.16	0.08 [1]
$\alpha_{g,s}$ / W m_p^{-2} K^{-1}	6.8	17.2	62 [2]

[1] Yagi and Kunii [1957] and Kunii and Smith [1960] (Eq. 15)

[2] Handley and Heggs [1968] and Stuke [1948] (Eq. 16 and 17)

Conclusions

In the case of non-circular channels the main mass transport resistances in a parallel passage reactor consist of mass transport from the bulk of the channel to the gauze wall and mass transport inside the bed. The mass transport resistance from the bulk of the channel to the gauze wall is negligible in the case of circular channels.

Transfer of momentum from the channel to the bed strongly enhances mass and heat transport through the gauze wall and mass and heat transfer from the gauze wall to the bed.

The mass transport resistance inside the bed can be quantified by means of an effective radial diffusion coefficient. The estimated value for the latter is comparable to values expected from correlations for classical fixed beds.

The heating of a parallel passage reactor can be described with a relatively simple two-dimensional model, with the effective radial thermal conductivity and the overall fluid-solid heat transfer coefficient as parameters. The effective radial thermal conductivity mainly consists of a static contribution at the conditions for industrial application of a parallel passage reactor. The main heat transport resistances in a parallel passage reactor are the heat transport resistance inside the bed and heat transfer resistance for the film surrounding the particle

Notation

A_c	channel cross section	m_c^2
a_i	roots of $J_1(a_i)=0$	
B	bed width	m_b
c	concentration	mol m_g^{-3}
c_m	mean concentration of tracer over the experimental section	mol m_g^{-3}
$C_{p,g}$	specific heat of gas	J kg^{-1} K^{-1}
$C_{p,s}$	specific heat of solid	J kg^{-1} K^{-1}
d_p	particle diameter	m_p
d_t	tube diameter	m_r
D_m	molecular diffusion coefficient	m_g^2 s^{-1}
D_r	effective radial diffusion coefficient	m_r^2 s^{-1}
G_b	superficial mass flow velocity in the bed	kg m_b^{-2} s^{-1}
G_c	superficial mass flow velocity in the channel	kg m_c^{-2} s^{-1}
J_o, J_1	Bessel functions	
k	mass transfer coefficient	m_r s^{-1}
L	bed length	m_b , m_c
r	radial position	m
R	tube radius	m
S_c	perimeter of the channel	m_c
S_b	specific area of the solid phase	m_p^2 m_s^{-3}
t	clock time	s
T_c	gas temperature in the channel	K
T_b	gas temperature in the bed	K
T_o	initial temperature of the heated gas	K
T_s	solid temperature	K
T_r	temperature of surroundings	K
u	superficial gas flow velocity	m_g^3 m_r^{-2} s
v	linear gas flow velocity	m_r s^{-1}
x	radial coordinate in the bed	m_b
z	axial coordinate	m_b , m_c

α_g	heat transfer coefficient for a film surrounding a particle	$W\ m_p^{-2}\ K^{-1}$
$\alpha_{g,s}$	overall fluid-solid heat transfer coefficient	$W\ m_p^{-2}\ K^{-1}$
ε	bed porosity	$m_g^3\ m_b^{-3}$
λ_{er}	effective radial thermal conductivity	$W\ m_b^{-1}\ K^{-1}$
λ_{er}°	static contribution to λ_{er}	$W\ m_b^{-1}\ K^{-1}$
λ_g	gas phase thermal conductivity	$W\ m_g^{-1}\ K^{-1}$
λ_s	solid phase thermal conductivity	$W\ m_p^{-1}\ K^{-1}$
μ_g	gas dynamic viscosity	$Pa\ s$
ρ_g	gas phase density	$kg\ m_g^{-3}$
ρ_s	solid phase density	$kg\ m_s^{-3}$
ϕ_t	radial heat flux	$W\ m_b^{-2}$

Nu	Nusselt number	$\alpha_g\ d_p\ \lambda_g^{-1}$
Re	Reynolds number	$u\ \rho_g\ d_p\ \mu_g^{-1}$
Pr	Prandl number	$\mu_g\ C_p\ \lambda_g^{-1}$
Sc	Schmidt number	$\mu_g\ \rho_g^{-1}\ D_m^{-1}$
Pe_r	Péclet number for radial dispersion based on particle diameter	$v\ d_p\ D_r^{-1}$
$Pe_{R,r}$	Péclet number for radial dispersion based on tube diameter	$v\ R\ D_r^{-1}$
$Pe_{L,r}$	Péclet number for axial dispersion based on tube diameter	$v\ R\ D_r^{-1}$
Ψ	dimensionless axial position	$z\ R^{-1}$
λ	dimensionless radial position	$r\ R^{-1}$
Φ	dimensionless tracer concentration	$c\ c_m^{-1}$

Subscripts

b	bed
c	channel
g	gas
p	particle
s	solid

References

Bischoff, K. B. and Levenspiel, O., 1962 A, *Chem. Eng. Sci.*, **17**, 245

Bischoff, K. B. and Levenspiel, O., 1962 B, *Chem. Eng. Sci.*, **17**, 257

Dixon, G.A. and Cresswell, D.L., 1979, *A. I. Ch. E. J.*, **25**, 663

Ergun, S., 1952, *Chem. Eng. Prog.*, **48**, 2, 89

Gunn, D.J., 1987, *Chem. Eng. Sci.*, **42**, 363

Handley, D. and Heggs, P.J , 1968, *Trans. Inst. Chem. Engrs.*, **46**, T251

Kunii, D. and Smith, J.M., 1960, *A. I. Ch. E. J.*, **6**, 71

Li, C.H. and Finlayson, B.A., 1977, *Chem. Eng. Sci.*, **32**, 1055

Marquardt, D.W., 1963, *J. Soc. Indust. Appl. Math.*, **2**, 431

N.A.G. Fortran Library Manual, 1991, Oxford U.K., D02N Integrations for stiff ordinary differential systems, I.S.B.N. 1-85206-070-0

Pohlenz, J.B. and Braun, A.O., Report EPA-600/7-83-048, 717; from gov. rep. announce index (US) 1984, **84**, (1), 132

Stuke, B., 1949, *Angewandte Chemie*, **B20**, 262

Yagi, S. and Kunii, D., 1957, *A. I. Ch. E. J.*, **3**, 373

Figure captions

Figure 1: The gauze construction of the model reactor

Figure 2: Maximum tracer concentration as function of the radial coordinate for two different axial positions

Figure 3: Superficial gas flow velocity in the bed as function of the radial coordinate for trilobes and spheres and a channel gas flow velocity of 7 m s^{-1}

Figure 4: Superficial gas flow velocity in the bed as function of the radial coordinate for trilobes and spheres and a channel gas flow velocity of 20 m s^{-1}

Figure 5: Steady state radial concentration profile during continuous tracer injection in the upper corner of a triangular channel, granules as packing material and a channel gas flow velocity of 7 m s^{-1}

Figure 6: Steady state radial concentration profile during continuous tracer injection in the upper corner of a triangular channel, granules as packing material and a channel gas flow velocity of 20 m s^{-1}

Figure 7: Steady state radial concentration profile during continous tracer injection in the upper side of a circular channel, granules as packing material and a channel gas flow velocity of 20 m s^{-1}

Figure 8: Steady state radial concentration profile; + : observed dimensionless gas phase concentrations; the full curve is from regression of the experimental data to the model (Equations 1 to 3)

Figure 9: solid phase temperature versus time; + : observed solid phase temperatures; the full curve is from regression of the complete set of experimental data to the model (Equations 7 to 14)

Figure 1

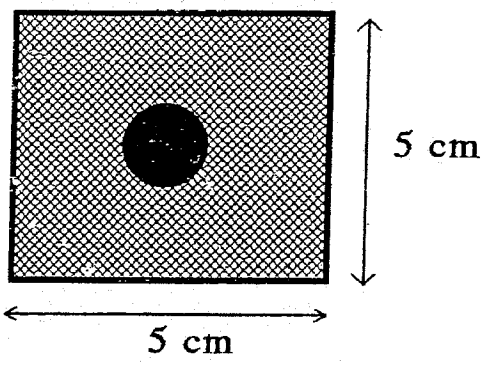

front and back view

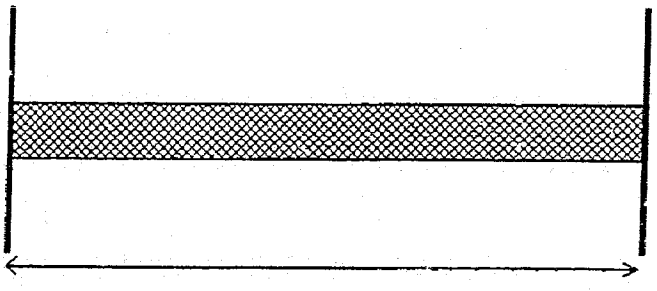

50 cm

side view

Figure 2

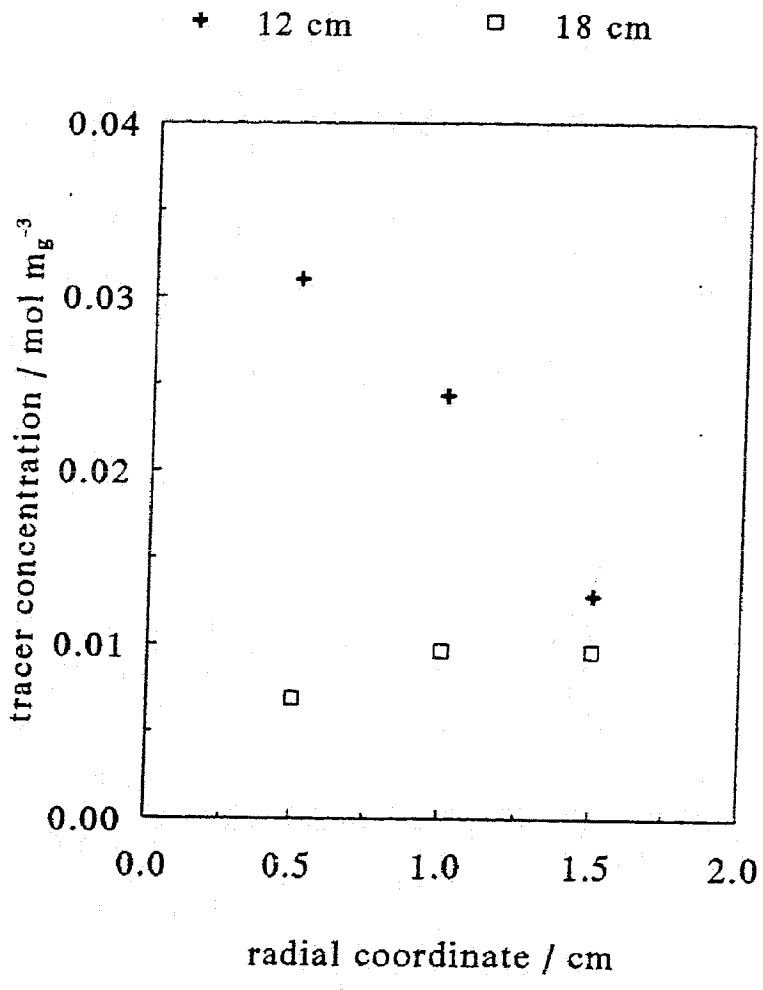
12 cm
18 cm
0.04
0.03
0.02
0.01
0.00
0.0
0.5
1.0
1.5
2.0
tracer concentration / mol m_g^{-3}
radial coordinate / cm

Figure 3

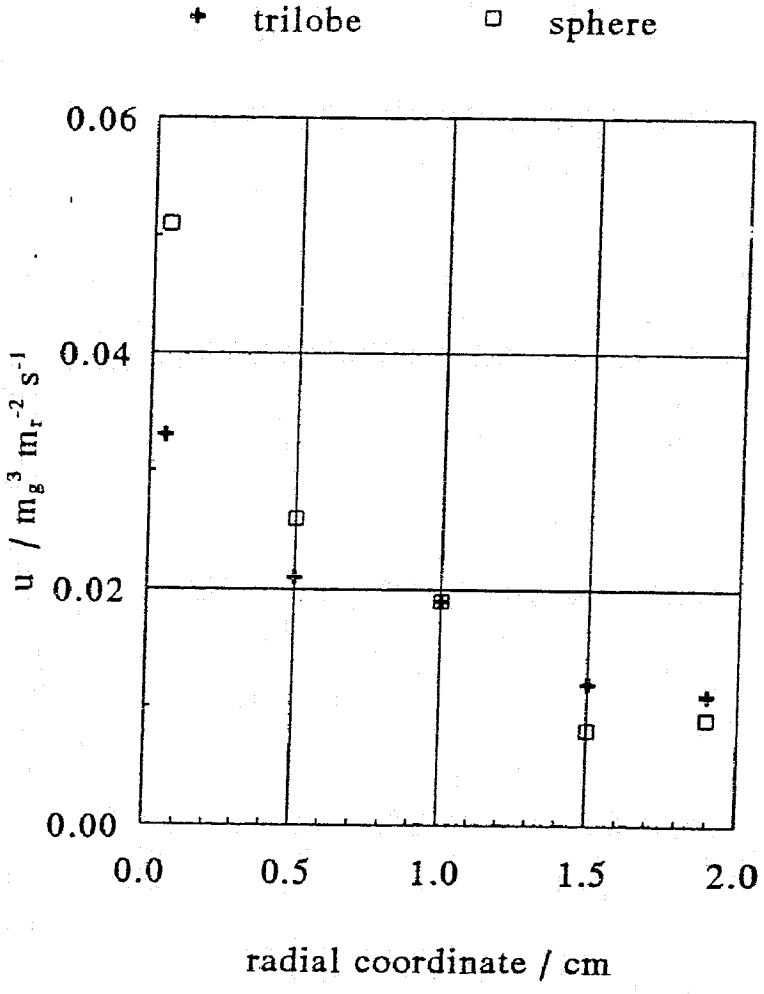
trilobe
sphere
0.06
0.04
0.02
0.00
u / m_g^3 m_r^{-2} s^{-1}
0.0
0.5
1.0
1.5
2.0
radial coordinate / cm

Figure 4

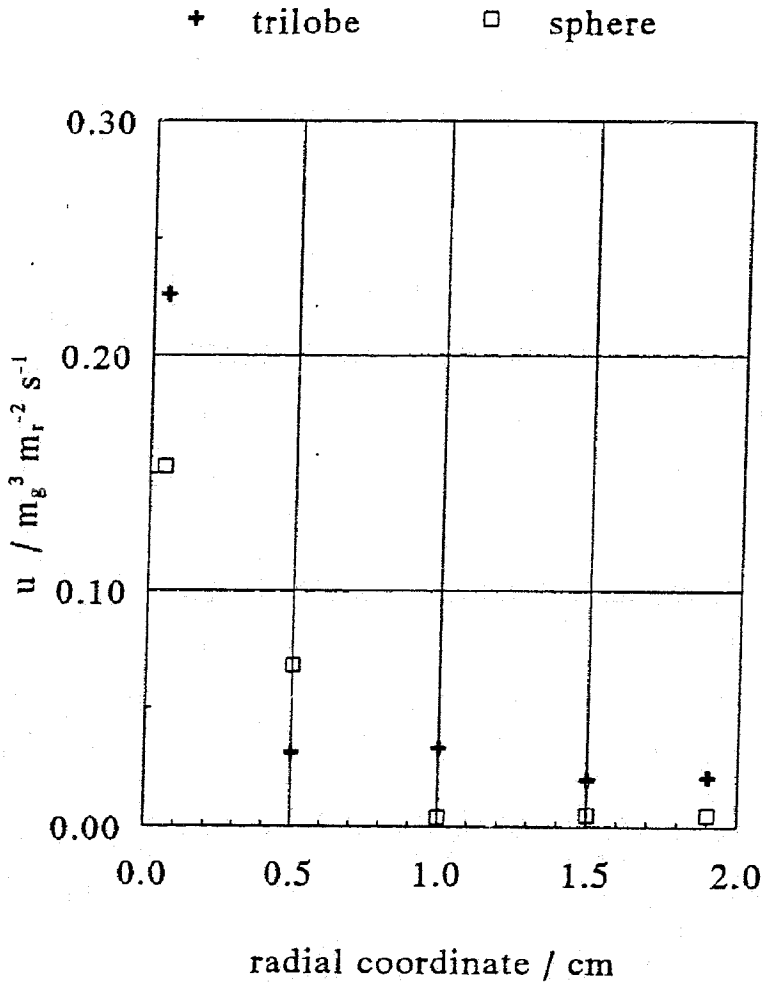
+ trilobe
□ sphere
0.30
0.20
0.10
0.00
u / m_g^3 m_r^{-2} s^{-1}
0.0
0.5
1.0
1.5
2.0
radial coordinate / cm

Figure 5

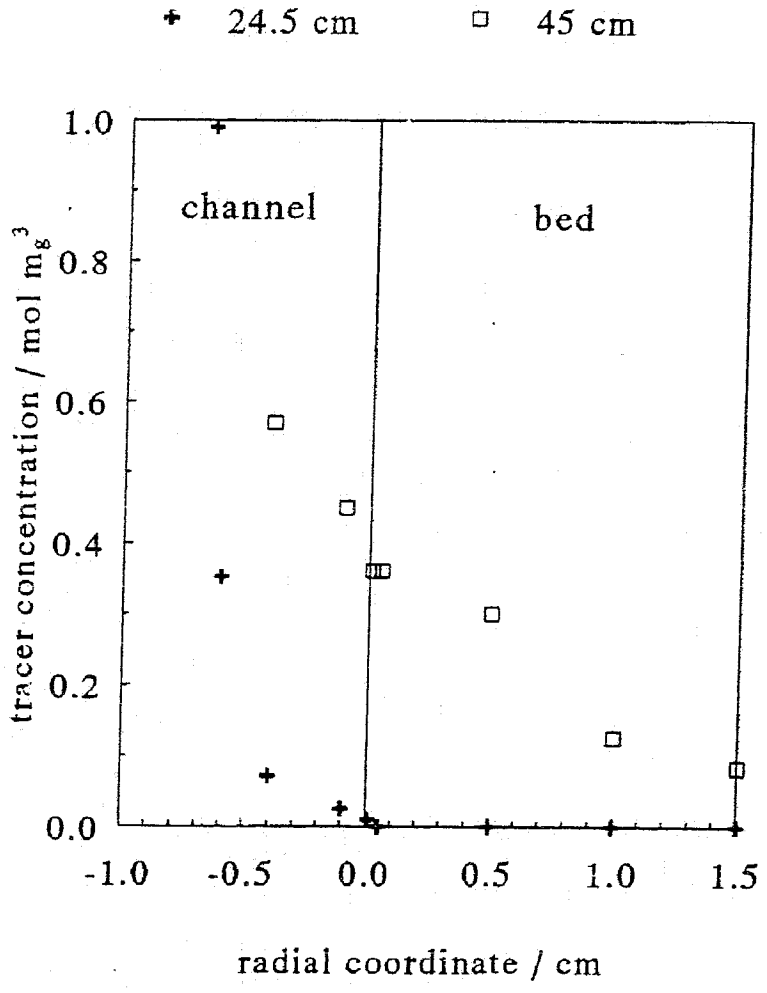
24.5 cm
45 cm
channel
bed
tracer concentration / mol m$_g^3$
1.0
0.8
0.6
0.4
0.2
0.0
-1.0
-0.5
0.0
0.5
1.0
1.5
radial coordinate / cm

Figure 6

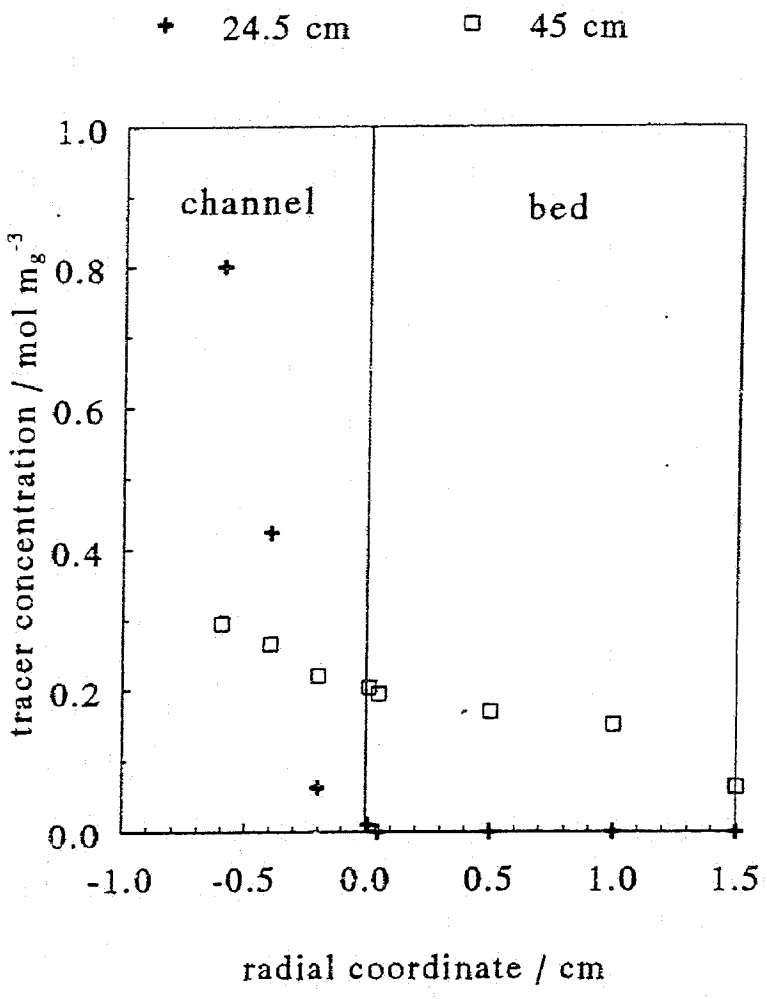
24.5 cm
45 cm
channel
bed
1.0
0.8
0.6
0.4
0.2
0.0
-1.0
-0.5
0.0
0.5
1.0
1.5
tracer concentration / mol m$_g^{-3}$
radial coordinate / cm

Figure 7

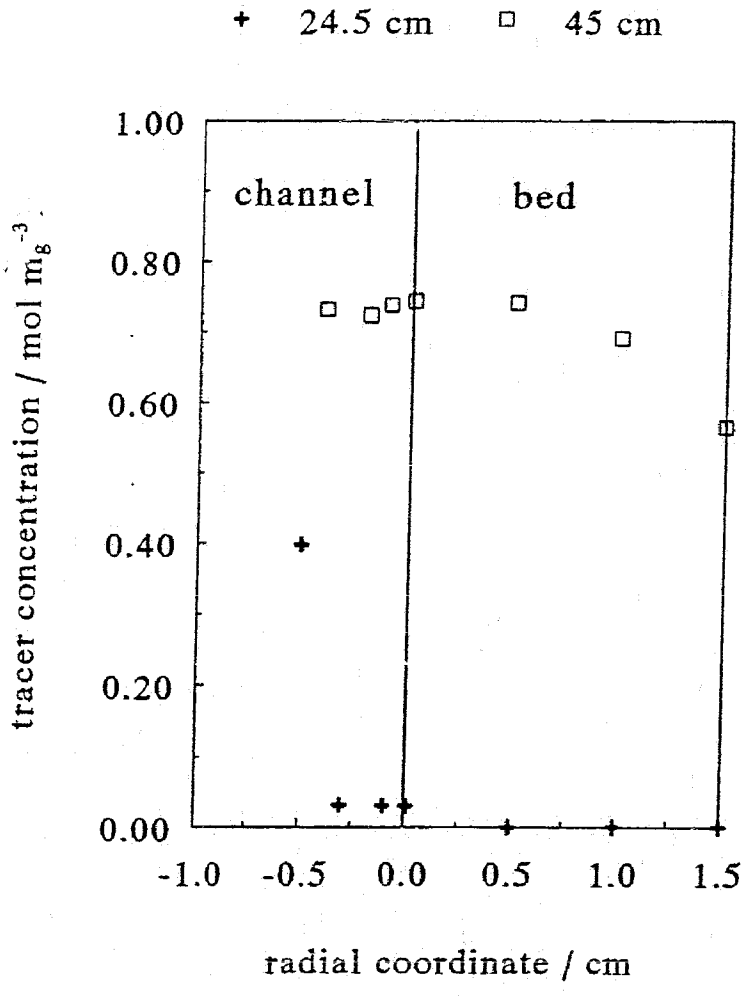
+ 24.5 cm
□ 45 cm
channel
bed
1.00
0.80
0.60
0.40
0.20
0.00
-1.0
-0.5
0.0
0.5
1.0
1.5
tracer concentration / mol m_g^{-3}
radial coordinate / cm

Figure 8

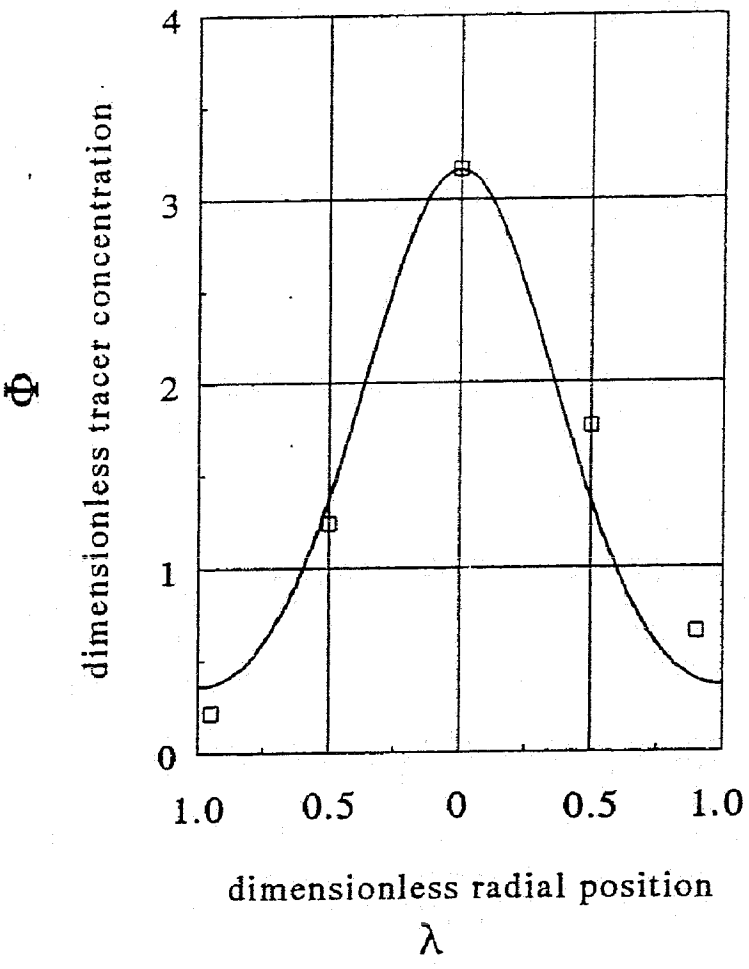
4
3
2
1
0
Φ
dimensionless tracer concentration
1.0
0.5
0
0.5
1.0
dimensionless radial position
λ

Figure 9